

Effect of Oxidation Temperature on Magnetron Sputtered Zirconium Niobium Films

Bukke Gopal Naik ¹, Sangaraju Venkata Jagadeesh Chandra ^{2,*} , Chanamolu Swathi ³, Suda Uthanna ^{1,*}

¹ Department of Physics, Sri Venkateswara University, Tirupati – 517 502, India; dr.sangaraju@gmail.com (B.G.N.);

² Department of Electronics and Communication Engineering, Vignan's Institute of Information Technology, Visakhapatnam - 530 046, India; svjchandra@gmail.com (S.V.J.C.);

³ Nanotechnology Laboratory, Department of Instrument Technology, Andhra University, Visakhapatnam, Andhra Pradesh, India; chandusvj@yahoo.com (C.S.);

* Correspondence: svjchandra@gmail.com(S.V.J.C.), uthanna.suda@gmail.com (S.U.);

Scopus Author ID 24076172500

Received: 3.04.2021; Revised: 1.05.2021; Accepted: 6.05.2021; Published: 18.06.2021

Abstract: Thermal treatment was performed on DC magnetron sputtered zirconium niobium ($Zr_{0.7}Nb_{0.3}$) films in the oxygen-enriched environment at different temperatures in the range 400 – 700°C to transform from $Zr_{0.7}Nb_{0.3}$ to $Zr_{0.7}Nb_{0.3}O_2$ films. The films oxidized at 700°C were of tetragonal $Zr_{0.7}Nb_{0.3}O_2$ with a crystallite size of 22 nm. There was a significant increase in the optical transmittance of the $Zr_{0.7}Nb_{0.3}O_2$ films from 75% to 90%, and eventually, the optical band gap also increased from 4.32 to 4.61 eV by increasing the oxidation temperature from 400 to 700 °C, respectively. The metal-oxide-semiconductor stacks of Al/ $Zr_{0.7}Nb_{0.3}O_2$ /p-Si showed higher dielectric constant values with improved interface quality at oxide/Si stack upon thermal oxidation at 700°C with relatively lower leakage currents.

Keywords: $Zr_{0.7}Nb_{0.3}O_2$ thin films;structure; FTIR; XPS;optical;dielectric constant; leakage currents.

© 2021 by the authors. This article is an open-access article distributed under the terms and conditions of the Creative Commons Attribution (CC BY) license (<https://creativecommons.org/licenses/by/4.0/>).

1. Introduction

Zirconium oxide (ZrO_2) is familiarly known as zirconia. It is prominent material for device applications because of its high mechanical strength, fracture toughness, thermal insulation, high transparency, and resistance to erosion[1]. On the other hand, ZrO_2 shows good thermal stability with silicon and has a high dielectric constant is considered a promising candidate for conventional very large-scale integration processing [2]. Its high refractive index, large bandgap, insignificant optical losses, and high transparency in the visible region made it useful for high reflectance mirrors, active optoelectronic devices, and broadband filters [3-5]. In recent years, much attention is focused on the doped zirconium oxide thin films for optoelectronic devices. Hydrogenated zirconium oxide is a potential candidate for application in solid-state ionic energy devices [6]. Aluminum-doped zirconium oxide leads to the tuning of the refractive index for optoelectronic applications [7]. Gold doped zirconium oxide coatings realized strong visible light absorption due to localized surface plasmon resonance for use in plasmonic devices such as lenses, switches, and waveguides [8]. Copper doped ZrO_2 nanoparticles grab attraction for photocatalytic applications [9]. Atomic layer deposited CeO_2 - ZrO_2 films are potential for solid-state oxide fuel cells [10], HfO_2 - ZrO_2 films in electrostatic supercapacitors [11], ZrO_2 - TiO_2 films as corrosion resistance [12], and sensing of oxygen, hydrogen, methane, and carbon monoxide gases [13]. Doping of yttrium /calcium in zirconium

oxide films spread a broad range of refractive index, which is attractive for wide optical applications [10]. There was a significant role of niobium compound films for various societal applications [14-16]. Zirconium niobium alloy oxide finds multiple applications for microelectronics and optical devices [17, 18]. The addition of niobium (Nb) increases the Ti-Zr alloy's stability and biologic corrosion resistance [19]. Santos *et al.* [20] deposited Nb-doped ZrO₂ (Nb = 19 - 50 wt.%) films by spark anodization method and noticed that the films were a mixed phase of hexagonal zirconium, tetragonal along with monoclinic ZrO₂ and tetragonal Nb₂O₅, and the grain size increased with the increase of niobium content.

In this investigation, the influence of oxidation temperature on the structural, optical, and electrical properties of Zr_{0.7}Nb_{0.3}O₂ films was reported systematically.

2. Materials and Methods

Zirconium niobium oxide (Zr_{0.7}Nb_{0.3}O₂) films were deposited on quartz and p-Type silicon substrates by DC reactive magnetron sputtering technique. The sputtering system employed for the deposition of Zr_{0.7}Nb_{0.3}O₂ films was the diffusion pump backup by a rotary pump. Pressure in the sputter chamber was measured with Pirani - Penning gauge combination. The sputter deposition conditions fixed for the preparation of Zr_{0.7}Nb_{0.3}O₂ films were given in the following table.

Table 1. Conditions for preparation of zirconium niobium films by DC magnetron sputtering.

Deposition method	DC magnetron sputtering
Sputter target	Zr _{0.7} Nb _{0.3} (99.95% pure) target
Target to substrate distance	60 mm
Substrates	Quartz and p- Silicon
Substrate temperature	30 °C
Sputter power	80 Watt
Ultimate pressure	5x10 ⁻⁶ Torr
Sputter pressure	6x10 ⁻³ Torr

The Zr_{0.7}Nb_{0.3} films were oxidized at different temperatures in the range 500-700 °C to get Zr_{0.7}Nb_{0.3}O₂ films. The thickness of the deposited films measured with the Dektak depth profilometer was in the range of 90-110 nm. The Zr_{0.7}Nb_{0.3}O₂ films elemental composition was analyzed by using an energy dispersive X-ray analyzer (Oxford Instruments Inca Penta FETX3) attached to the scanning electron microscope (Carl Zeiss model EVO MAIS). Chemical bonding configuration was analyzed with Fourier transform infrared spectrophotometer (Thermo-Nicolet model 6700) and core level binding energies by X-ray photoelectron spectroscopy (Physical Electronics Model PHI 5700). The structure of the films was studied with an X-ray diffractometer (X'pert Pro PAN Analytical) with Cu K α radiation ($\lambda = 0.15406$ nm). The optical transmittance of Zr_{0.7}Nb_{0.3}O₂ films formed on quartz substrates was recorded in the wavelength range 200-1000 nm using JASCO spectrophotometer (model V570) UV-Vis-NIR double beam spectrophotometer to determine the optical band gap and refractive index of the films. Metal-oxide-semiconductor (MOS) capacitors with Al/Zr_{0.7}Nb_{0.3}O₂/Si stacks were fabricated using a shadow mask of circular capacitors of 300 μ m diameter by depositing aluminum metal on the top of the Zr_{0.7}Nb_{0.3}O₂ films. The capacitance-voltage characteristics of the Zr_{0.7}Nb_{0.3}O₂ based MOS stacks were measured by using MIOKI (model 3532-50) LCR meter. The current-voltage characteristics were measured using Hewlett Packard (model hp 4140B) pA meter.

3. Results and Discussion

3.1. Chemical Composition by Energy Dispersive X-ray Analysis.

The chemical composition of the films formed on silicon substrates was determined by energy-dispersive X-ray (EDAX) analysis. Figure 1 shows the EDAX spectra of as-deposited zirconium niobium films, and the films oxidized at 600 °C and 700 °C. The metallic zirconium niobium film spectra consist only of the characteristic zirconium and niobium peaks along with silicon peaks. The metallic zirconium niobium films with the chemical content of zirconium 67.8 at. % and niobium 32.2 at. % that is $Zr_{0.68}Nb_{0.32}$. The films oxidized at temperatures of 600°C and 700 °C have contained the peaks of zirconium, niobium, and oxygen. The chemical composition of the films was determined from the intensity of the peaks and their sensitivity factors and the achieved data is compiled in Table 2. It is clear from the table that the content of oxygen increased with an increase in oxidation temperature.

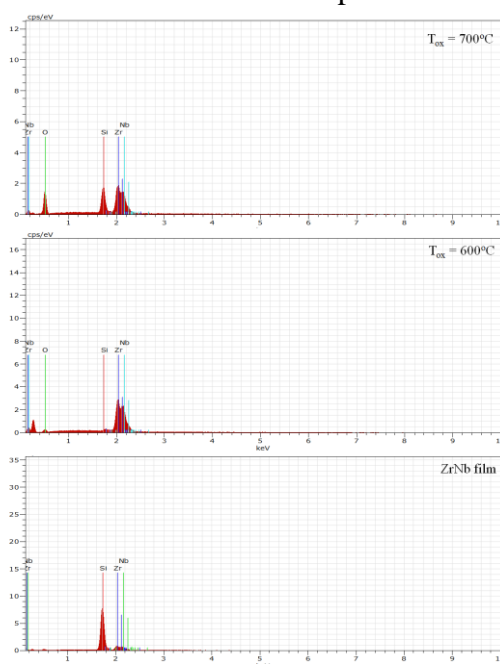


Figure 1. EDAX spectra of as-deposited and thermally oxidized $Zr_{0.7}Nb_{0.3}O_2$ films.

Table 2. Chemical composition of $Zr_{0.7}Nb_{0.3}O_2$ films determined by EDAX.

Oxidation temperature	Chemical composition (at.%) (EDAX)		
	Zirconium	Niobium	Oxygen
As-deposited	67.8	32.2	---
500 °C	30.1	13.7	56.2
600 °C	25.7	11.2	63.1
700 °C	23.6	10.3	66.1

The films oxidized at 500 °C consist of significant metallic zirconium (Zr) and niobium (Nb) phases (hence we are not showing the spectra here). The films oxidized at 600 °C showed the content of zirconium 25.7 at.%, niobium 11.2 at.%, and oxygen 63.1 at.% that is $Zr_{0.7}Nb_{0.3}O_2$ along with zirconium and niobium metallic phases. At oxidation temperature of 700 °C and above showed the composition of zirconium 23.6 at. %, niobium 10.3 at. % and oxygen 66.1 at. % indicated the growth of $Zr_{0.7}Nb_{0.3}O_2$ with the absence of metallic zirconium and niobium phases. It revealed that the films oxidized at a temperature of 700 °C were $Zr_{0.7}Nb_{0.3}O_2$.

3.2. Structural properties.

Figure 2 shows the X-ray diffraction profiles of the as-deposited and oxidized $Zr_{0.7}Nb_{0.3}$ films. No diffraction reflections were seen in the as-deposited, and oxidized $Zr_{0.7}Nb_{0.3}$ films up to 600 °C were amorphous.

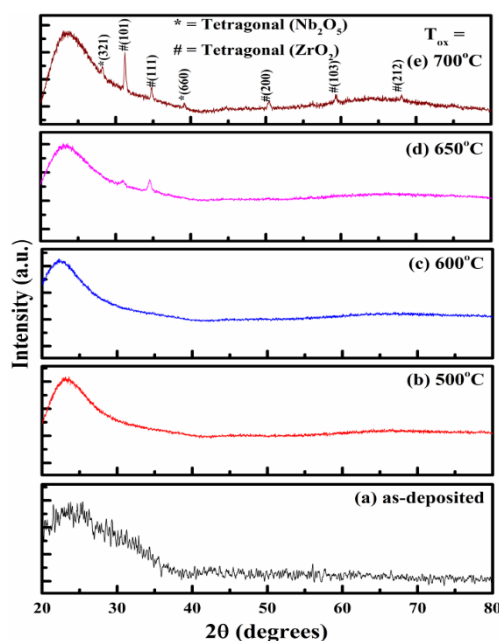


Figure 2. XRD profiles of as-deposited and thermally oxidized $Zr_{0.7}Nb_{0.3}O_2$ films.

The films oxidized at 650 °C showed the diffraction peaks at $2\theta = 31.24^\circ$ and 34.78° related to (101) and (111) reflections of Nb_2O_5 , and it is in accordance with JCPDS card No. 72.1484. It indicated that the films oxidized at 650 °C were polycrystalline in nature. The films oxidized at 700 °C showed the diffraction peaks at $2\theta = 28.24^\circ, 39.09^\circ, 50.43^\circ, 59.34^\circ,$ and 68.06° correspond to (321), (660), (200), (103) and (212) reflections of tetragonal ZrO_2 in accordance with the JCPDS card No. 42-1164. There was a shift in the 2θ value of about 0.3 - 0.5° in the diffraction peaks when compared with compounds of ZrO_2 and Nb_2O_5 , which revealed that the niobium substituted the zirconium in ZrO_2 and formed with tetragonal structured $Zr_{0.7}Nb_{0.3}O_2$. Energy-dispersive X-ray analysis also confirmed that the films oxidized films at 700 °C were of $Zr_{0.7}Nb_{0.3}O_2$. Santos *et al.* [20] reported that the niobium-doped ZrO_2 films (Nb = 20 – 50 wt. %) deposited by the electrochemical method were mixed phases of hexagonal zirconium, monoclinic and tetragonal phase ZrO_2 with different crystallographic phases of Nb_2O_5 . The crystallite size (D) of the films was calculated using Debye-Scherrer’s relation,

$$D = 0.9 \lambda / \beta \cos\theta \quad \text{--- (1)}$$

where λ is the wavelength of copper X-ray radiation, β the full width at half maximum intensity of diffraction peak, and θ the diffraction angle. The crystallite size of the films increased from 8 nm to 22 nm with an increase of oxidation temperature from 650 °C to 700 °C, respectively. The increase in the crystallite size with oxidation temperature was due to an improvement in the crystallinity of films. Dislocation density (δ) and strain (ε) developed in the films were calculated from the X-ray diffraction peaks employing the relation,

$$\delta = 1/D^2 \quad (2)$$

and

$$\varepsilon = \beta \cos\theta/4 \quad (3)$$

Dislocation density and strain developed in the films were calculated from the X-ray diffraction peaks decreased from 27.7×10^{16} lines/m² to 2.0×10^{16} lines/m², and strain decreased from 21.2×10^{-3} to 5.9×10^{-3} with the increase of oxidation temperature from 650 °C to 700 °C, respectively. The decrease in the dislocation density and strain with an increase of crystallite size was observed along with the increase of oxidation temperature.

3.3. Surface morphology.

The surface morphology of the films was studied using a scanning electron microscope. Figure 3 shows the scanning electron micrographs of as-deposited Zr_{0.7}Nb_{0.3} films and the films oxidized at different temperatures. The grain size of the Zr_{0.7}Nb_{0.3}O₂ films increased from 97 nm to 118 nm with an increase of oxidation temperature from 600 °C to 700 °C. With the increase of oxidation temperature, there was a subsequent increase in the grain size of Zr_{0.7}Nb_{0.3}O₂ films.

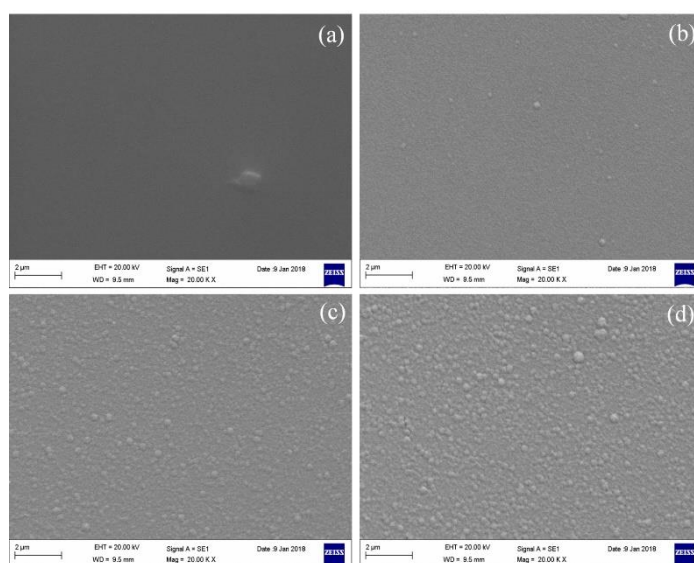


Figure 3. SEM images Zr_{0.7}Nb_{0.3}O₂ films of (a) as-deposited; thermally oxidized at (b) 500°C; (c) 600°C; (d) 700°C.

3.4. X-ray photoelectron spectroscopic studies.

Figure 4 shows survey (Figure 4a) and narrow scan XPS spectra Zr_{0.7}Nb_{0.3} films oxidized at 700 °C. Narrow scan spectrum of zirconium Zr 3d (Figure 4b), niobium Nb 3d (Figure 4c), and oxygen O 1s (Figure 4d) extracted from Zr_{0.7}Nb_{0.3}O₂ films. All these spectra revealed the existence of Nb along with the Zr and O₂. The core-level binding energies located at about 180.35 eV and 182.73 eV related to the zirconium Zr 3d_{3/2} and Zr 3d_{5/2} due to spin-orbit splitting with separation in the energy of 2.38 eV revealed the Zr⁴⁺ state ZrO₂ [19, 20]. The binding energies are seen at 205.29 eV, and 208.11 eV correspond to niobium Nb 3d_{3/2} and Nb 3d_{5/2}, and the energy separation of 2.82 eV revealed the Nb⁵⁺ state that is niobium oxide [21, 22]. On the other hand, Figure 4d showed the O 1s core-level binding energy at 29.1 eV, which is the possible evidence for the stoichiometric zirconium niobium oxides films. It was noted that the core level binding energies were shifted about 0.3 eV in Zr 3d and Nb 3d, which confirms that the grown films were indicated Zr_{0.7}Nb_{0.3}O₂ films.

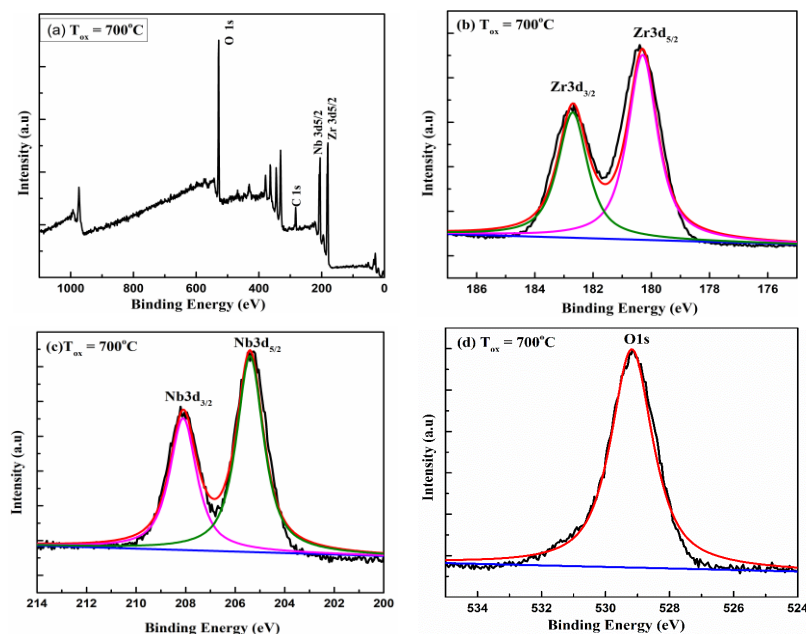


Figure 4. XPS spectrum of $Zr_{0.7}Nb_{0.3}O_2$ films oxidized at $700^\circ C$: (a) survey scan; narrow scan spectra of (b) Zr 3d; (c) Nb 3d; (d) O 1s.

3.5. Fourier transform infrared studies.

The chemical binding configuration of the films formed on p- silicon was examined with Fourier transform infrared spectroscope. Fourier transforms infrared transmittance spectra of the films oxidized at different temperatures are shown in Figure 5. Metallic $Zr_{0.7}Nb_{0.3}$ films did not show absorption bands in the spectrum. The films oxidized at $500^\circ C$ exhibited the absorption bands at 505 cm^{-1} , 600 cm^{-1} , 620 cm^{-1} , 740 cm^{-1} and 1110 cm^{-1} . The band located at 515 cm^{-1} and 600 cm^{-1} were attributed to the antisymmetric stretching mode of Zr-O and 740 cm^{-1} due to the symmetric stretching mode of Zr - O in ZrO_2 films [23]. The absorption bands were seen at 620 cm^{-1} , and 1110 cm^{-1} were the stretching vibration mode of Nb - O of Nb_2O_5 [24]. Further increase of oxidation temperature intensity of absorption band increased due to improved crystallinity of the $Zr_{0.7}Nb_{0.3}O_2$ films. In the case of the films oxidized at $700^\circ C$, the absorption band 505 cm^{-1} was shifted to 515 cm^{-1} . It is also confirmed that the oxidized films at around $700^\circ C$ were of $Zr_{0.7}Nb_{0.3}O_2$ films.

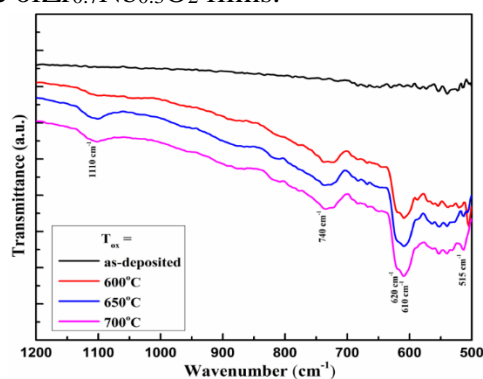


Figure 5. FTIR transmittance spectra of as-deposited and thermally oxidized $Zr_{0.7}Nb_{0.3}O_2$ films.

3.6. Optical properties.

Figure 6 shows the optical transmittance spectra of the films oxidized at different temperatures. The optical transmittance of the films increased from 75 to $\sim 90\%$ in the visible region with the increase of oxidation temperature from $400^\circ C$ to $750^\circ C$.

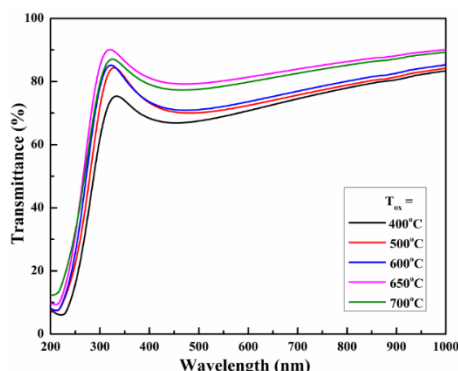


Figure 6. Optical transmittance spectra of as-deposited and thermally oxidized $Zr_{0.7}Nb_{0.3}O_2$ films.

The low transmittance at oxidation temperatures at 400 °C was due to the incomplete transformation of $Zr_{0.7}Nb_{0.3}$ films into $Zr_{0.7}Nb_{0.3}O_2$ films and also the presence of some defects in the targeted oxide films [25, 26]. The fundamental absorption edge of the films shifted towards the lower wavelength side due to the filling of oxygen ion vacancies in the $Zr_{0.7}Nb_{0.3}O_2$ films. The optical absorption coefficient (α) was determined from the optical transmittance (T) and thickness (t) of the films using the relation

$$\alpha = - (1/t) \ln (T) \tag{4}$$

In order to determine the optical band gap (E_g), the optical absorption data of the films was fitted to the relation [27],

$$(\alpha hv)^2 = A (hv - E_g) \tag{5}$$

where hv is the photon energy and E_g the optical bandgap. The optical bandgap of the films was determined from Tauc's plots. Figure 7 shows the plots of $(\alpha hv)^2$ versus photon energy of $Zr_{0.7}Nb_{0.3}O_2$ films oxidized at different temperatures.

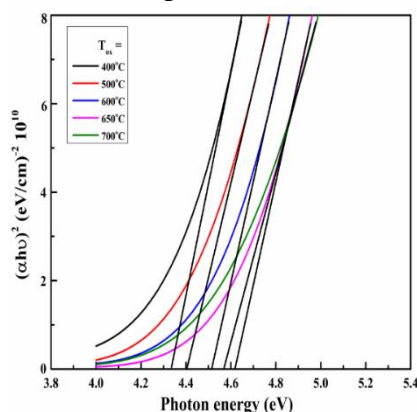


Figure 7. Plots of $(\alpha hv)^2$ versus photon energy of thermally oxidized $Zr_{0.7}Nb_{0.3}O_2$ films.

The optical bandgap of the films oxidized at 400 °C was 4.32 eV, and it increased from 4.40 eV to 4.61 eV with an increase of oxidation temperature from 500 °C to 700 °C. The low optical bandgap in the films oxidized at low temperatures was due to oxygen deficiency, that is, the excess of metallic zirconium and niobium along $Zr_{0.7}Nb_{0.3}O_2$. The $Zr_{0.7}Nb_{0.3}O_2$ films oxidized at 700 °C showed a large bandgap of 4.61 eV. As the oxidation temperature increases, the thermal energy given accelerates to fill the oxygen ion vacancies, thereby increasing the optical bandgap. Larijani *et al.*[28] noticed that DC magnetron sputtered zirconium films transformed into ZrO_2 with an optical band gap of 4.08 eV at the oxidation of 450°C and 5.15 eV in electron beam deposited films [29]. In the case of Nb_2O_5 films deposited by RF magnetron sputtering, the optical band gap decreased from 3.62 eV to 3.07 eV with an increase of annealing in air at temperatures from 30°C to 900°C [30] and increased from 3.29 eV to 3.46

eV with an increase of sputter power [31]. The optical bandgap of TiO₂ films also increased with annealing temperature [32].

3.7. Electrical and dielectric properties.

Figure 8 shows the capacitance-voltage (C-V) curves of the Al/Zr_{0.7}Nb_{0.3}O₂/Si stacks of thermally oxidized Zr_{0.7}Nb_{0.3} thin film with the thickness of ~ 99 nm. The accumulation capacitance value of the Zr_{0.7}Nb_{0.3}O₂/Si stacks was decreased from ~ 0.69 to 0.61 μF/cm² by increasing oxidation temperature from 500 to 700 °C, respectively. The possible reason for this reduction in accumulation capacitance could be due to the strengthening of the interfacial SiO₂ layer at Zr_{0.7}Nb_{0.3}O₂/Si stacks [33, 34]. Pure ZrO₂/Si stacks struggled with low dielectric properties and eventually unstable interface at higher temperatures [35], whereas here we observed the stable C-V curve of Zr_{0.7}Nb_{0.3}O₂/Si stacks after the thermal treatment at 700 °C. This is the direct evidence of improvement in the thermal stability of Zr_{0.7}Nb_{0.3}O₂/Si stacks. Besides, there was a significant positive shift in the C-V curve of the stacks oxidized at the temperature of 700 °C, which might be due to the filling of oxygen vacancies in the oxide layer and the reduction in fixed charges at the oxide/semiconductor interface [36].

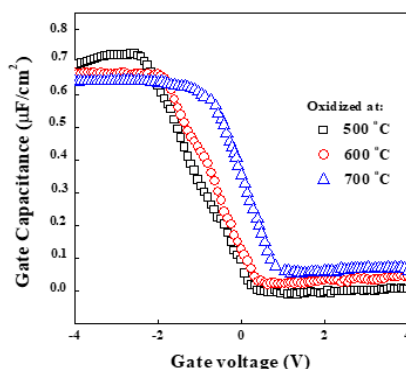


Figure 8. Capacitance - voltage characteristics of Al/Zr_{0.7}Nb_{0.3}O₂/Si capacitors formed at different oxidation temperatures.

The dielectric constant (ϵ_r) of the films was calculated from the C-V measurements using the formula

$$\epsilon_r = Ct/\epsilon_0A \quad \text{--- (6)}$$

where C is the capacitance, ‘t’ the thickness of the dielectric, A the area of the electrode, and ϵ_0 the permittivity of the free space. The dielectric constant of the Al/Zr_{0.7}Nb_{0.3}O₂/Si stacks annealed at 500 °C was 9 and increased to 11 and 14 by increasing the annealing temperature 600 °C and 700 °C, respectively. Figure 9 shows the current-voltage characteristics of

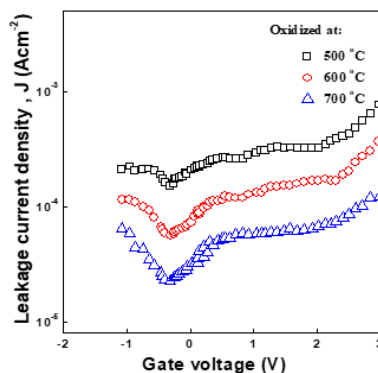


Figure 9. Current-voltage characteristics of Al/Zr_{0.7}Nb_{0.3}O₂/Si capacitors formed at different oxidation temperatures.

Al/Zr_{0.7}Nb_{0.3}O₂/p-Si stacks annealed at 500, 600, and 700°C. The leakage current density was decreased from 2x10⁻⁴A/cm² to ~3x10⁻⁵A/cm² by increasing the thermal oxidation temperature from 500 °C to 700 °C, respectively. The reduction in the leakage current value might be due to the strengthening of the stable SiO₂ layer at high-k/Si stacks [36]. The leakage current densities versus voltage curves combine linear and non-linear regions due to the current assimilation mechanism, such as Schottky Poole- Frenkel. The shifting of lower leakage current density value at the applied gate voltage of 0 V is under investigation.

4. Conclusions

Thin films of zirconium niobium oxide (Zr_{0.7}Nb_{0.3}O₂) were prepared by thermal oxidation of metallic DC magnetron sputtered Zr_{0.7}Nb_{0.3} films onto quartz and p- silicon substrates held at room temperatures. The oxidation temperature controls the growth of Zr_{0.7}Nb_{0.3}O₂ films. EDAX analysis studies showed that the films oxidized at temperatures less than 600 °C were of mixed-phase of metallic zirconium and niobium along with Zr_{0.7}Nb_{0.3} whereas those oxidized at 700 °C were tetragonal structures Zr_{0.7}Nb_{0.3}O₂. Fourier transform infrared spectroscopy and X-ray photoelectron spectroscopic studies confirmed the presence of characteristic vibration modes of Zr-O and Nb-O and core level binding energies related to Zr_{0.7}Nb_{0.3}O₂ upon high-temperature oxidation. The dielectric constant value and bottom interfacial properties of Al/Zr_{0.7}Nb_{0.3}O₂/Si, MOS stacks were improved by increasing oxidation temperature from 500 °C to 700 °C, because of filling the oxygen vacancies in and around the oxide layer. The leakage currents were also reduced to the order of 10⁻⁵ for the stacks oxidized at 700 °C. The thermal stability of the investigated oxide layer with Si substrate was improved by the addition of Nb into Zr. Further investigations may give more attractive results of this high-k alloy.

Funding

This research received no external funding.

Acknowledgments

One of the authors, Dr. S. Uthanna, is thankful to the University Grants Commission, New Delhi, India, for the UGC-BSR Faculty Fellowship award.

Conflicts of Interest

The authors declare no conflict of interest.

References

1. Huan, L.; Han, G.; Liu, Y.; Hao, Y. High Mobility Ge pMOSFETs with ZrO₂ Dielectric: Impacts of PostAnnealing. *Nanoscale Res Lett.* **2019**, *14*, <https://doi.org/10.1186/s11671-019-3037-4>.
2. Kondaiah, P.; Jagadeesh Chandra, S.V.; Fortunato, E.; Choi C.J.; Mohan Rao, GRama Koti Reddy, D.V.; Uthanna, S. Substrate temperature influenced ZrO₂ films for MOS devices. *Surf. Inter. Anal.* **2020**, *52*, 541-546, <https://doi.org/10.1002/sia.6775>.
3. Horti, N.C.; Kamatagi, M.D.; Nataraj, S.K.; Wari, M.N.; Inamdar, S.R. Structural and optical properties of zirconium oxide (ZrO₂) nanoparticles: effect of calcination temperature. *Nano Exp.* **2020**, *1*, 010022, <https://doi.org/10.1088/2632-959X/ab8684>.

4. Dimitrov, O.; Stambolova, I.; Vassilev, S.; Lazarova, K.; Babeva, T.; Mladenova, R. Surface Features of ZrO₂ Sol-Gel Coatings Obtained by Polymer Modified Solution. *Mater.Proc.* **2020**, *2*, 1-8, <https://doi.org/10.3390/CIWC2020-06810>.
5. Thakar, K.; Saurabh, L. Optoelectronic and photonic devices based on transition metal dichalcogenides. *Mater. Res. Express* **2020**, *7*, 014002, <https://doi.org/10.1088/2053-1591/ab5c9c>.
6. Li, N.; Suzuki, M.; Abe, Y.; Kawamura, M.; Sasaki, K.; Itoh, H.; Suzuki, T. Effects of substrate temperature on the ion conductivity of hydrated ZrO₂ thin films prepared by reactive sputtering in H₂O atmosphere. *Solar Energy Mater. Solar Cells* **2012**, *99*, 160-165, <https://doi.org/10.1016/j.solmat.2011.03.037>.
7. Roy, M.; Kubacki, J.; Psiuk, B.; Wilczkiewicz, A.M.; Malarz, K.; Corti, A.; Pompella, A.; Szade, J. Photofunctionalization effect and biological ageing of PEEK, TiO₂ and ZrO₂ abutments material. *Mater. Sci. Engg. C* **2021**, *121*, 111823, <https://doi.org/10.1016/j.msec.2020.111823>.
8. Berlin, I.J.; Joy, K. Optical enhancement of Au doped ZrO₂ thin films by sol-gel dip coating method. *Physica B* **2015**, *457*, 182, <https://doi.org/10.1016/j.physb.2014.10.013>.
9. Alfeche, D.M.; Cervera, R.B. Highly conducting Sc and Y co-doped ZrO₂ thin film solid electrolyte on aporous Ni/YSZ electrode prepared via simple drop-coating method. *Ceram. Int.* **2020**, *46*, 10561-10567, <https://doi.org/10.1016/j.ceramint.2020.01.058>.
10. Arjun, A.; Dharr, A.; Raguram, T.; Rajni, K. S. Study of Copper Doped Zirconium Dioxide Nanoparticles Synthesized via Sol-Gel Technique for Photocatalytic Applications. *J. Inorgan. Organ. Polym. Mater.* **2020**, *30*, 4989-4998, <https://doi.org/10.1007/s10904-020-01616-4>.
11. Kim, K.D.; Lee, Y.H.; Gwon, T.; Kim, Y.T.; Kim, H.J.; Moon, T.; Hyun, S.D.; Park, H.W.; Park, M.H.; Hwang, C.S. Scale-up and optimization of HfO₂-ZrO₂ solid solution thin films for the electrostatic supercapacitors. *Nano Energy* **2017**, *39*, 390-399, <https://doi.org/10.1016/j.nanoen.2017.07.017>.
12. El-Lateef, H.M.A.; Khalif, M.M. Corrosion resistance of ZrO₂-TiO₂ nanocomposite multilayer thin films coated on carbon steel in hydrochloric acid solution. *Mater. Charact.* **2015**, *108*, 29-41, <https://doi.org/10.1016/j.matchar.2015.08.010>.
13. Simonenko, E.P.; Mokrushin, A.S.; Simonenko, N.P.; Voronov, V.A.; Kim, V.P.; Thachev, S.V.; Gubin, S.P.; Sevaslyanov, V.G.; Kuznetsov, N. Ink-jet printing of a TiO₂-10%ZrO₂ thin film for oxygen detection using a solution of metal alkoxoacetylacetonates. *Thin Solid Films* **2019**, *670*, 46-53, <https://doi.org/10.1016/j.tsf.2018.12.004>.
14. Wu, M.; Yu, S.; Wang, X.; Li, L. Influence of substrate temperature on the energy storage properties of bismuth magnesium niobium thin films prepared by magnetron sputtering. *Ceram. Internation.* **2021**, *47*, 8265-8270, <https://doi.org/10.1016/j.ceramint.2020.11.186>.
15. Senocak, T.C.; Ezirmik, K.V.; Aysin, F.; Ozek, N.S.; Cengiz, S. Niobium-oxynitride coatings for biomedical applications: Its antibacterial effects and in-vitro cytotoxicity. *Mater. Sci. Engg. C* **2021**, *120*, 111662, <https://doi.org/10.1016/j.msec.2020.111662>.
16. Khamseh, S.; Alibakhshi, E.; Ramezanzadeh, B.; GanjaeeSari, M.; Nezhad, A.K. Developing a Graphite like Carbon:Niobium thin film on GTD-450 stainless steel substrate. *Appl. Surf. Sci.* **2020**, *511*, 145613, <https://doi.org/10.1016/j.apsusc.2020.145613>.
17. Mokhtar, A.M.; Salem, K.E.; Allam, N.K. Multiple synergistic effects of Zr-alloying on the phase stability and photostability of black niobium oxide nanotubes as efficient photoelectrodes for solar hydrogen production. *Appl. Catal. B: Env.* **2021**, *287*, 119961, <https://doi.org/10.1016/j.apcatb.2021.119961>.
18. Mishchenko, O.; Ovchynnykov, O.; Kapustian, O.; Pogorielov, M. New Zr-Ti-Nb Alloy for Medical Application: Development, Chemical and Mechanical Properties, and Biocompatibility. *Materials* **2020**, *13*, 1306, <https://doi.org/10.3390/ma13061306>.
19. Ji, P.F.; Li, B.; Chen, B.H.; Wang, F.; MaX, W.; Zhang, Y.; Ma, M.Z.; Liu, R.P. Effect of Nb addition on the stability and biological corrosion resistance of Ti-Zr alloy passivation films. *Corrosion Sci.* **2020**, *170*, 108696, <https://doi.org/10.1016/j.corsci.2020.108696>.
20. Santos, J.S.; Strixino, F.T.; Pereira, E.C. The influence of experimental conditions on the morphology and phase composition of Nb-doped ZrO₂ films prepared by spark anodization. *Corrosion Sci.* **2013**, *73*, 99-105, <https://doi.org/10.1016/j.corsci.2013.03.029>.
21. Hong, J.H.; Choi, W.J.; Myoung, J.M. Microelectron. Properties of ZrO₂ dielectric layers grown by metalorganic molecular beam epitaxy. *Microelectron. Eng.* **2003**, *70*, 35-40, [https://doi.org/10.1016/S0167-9317\(03\)00388-5](https://doi.org/10.1016/S0167-9317(03)00388-5).

22. Maiti, C.K.; Dalapathi, G.K.; Chatterjee, S.; Samanta, S.K.; Varma, S.; Patil, S. Electrical properties of high permittivity ZrO₂ gate dielectrics on strained-Si. *Solid State Electron.* **2004**, *48*, 2235-2241, <https://doi.org/10.1016/j.sse.2004.04.012>.
23. Lee, S.H.; Kwon, J.D.; Park, J.S. Compositional and electrical modulation of niobium oxide thin films deposited by plasma-enhanced atomic layer deposition. *Ceram. Int.* **2017**, *43*, 6580-6584, <https://doi.org/10.1016/j.ceramint.2017.02.089>.
24. Mazur, M.; Synmanska, M.; Kaemarck, D.; Kalisz, M.; Wojcieszak, D.; Domaradzki, J.; Placido, F. Determination of optical and mechanical properties of Nb₂O₅ thin films for solar cells application. *Appl. Surf. Sci.* **2014**, *301*, 63-69, <https://doi.org/10.1016/j.apsusc.2014.01.144>.
25. Nakajima, K.; Baba, Y.; Noma R.; Kitano, M.; Kondo, J.N.; Hayashi, S.; Hara, M. Nb₂O₅·nH₂O as a Heterogeneous Catalyst with Water-Tolerant Lewis Acid Sites, *J. Am. Chem. Soc.* **2011**, *133*, 4224-4227, <https://doi.org/10.1021/ja110482r>.
26. Venkataiah, S.; Jagadeesh Chandra, S.V.; Chalapathi, U.; Ramana, Ch.V.V.; Uthanna, S. Oxygen partial pressure influenced stoichiometry, structural, electrical, and optical properties of DC reactive oxide films. *Sur. Inter. Anal.* **2021**, *53*, 206-214, <https://doi.org/10.1002/sia.6902>.
27. Tauc, J. Optical Properties of Amorphous Semiconductors. In *Amorphous and Crystalline Semiconductors*, Plenum Press, NY, **1974**, https://doi.org/10.1007/978-1-4615-8705-7_4.
28. Larijani, M.M.; Hasani, E.; Safa, S. Annealing temperature effect on the optical properties of thermally oxidized nano-crystalline ZrO₂ thin films grown on glass substrates. *Appl. Surf. Sci.* **2014**, *290*, 490-494, <https://doi.org/10.1016/j.apsusc.2013.11.131>.
29. Ling, X.; Liu, X.; Wang, G.; Fan, Z. Influence of oxygen partial pressure on laser-induced damage resistance of ZrO₂ films in vacuum. *Vacuum* **2015**, *119*, 145-150, <https://doi.org/10.1016/j.vacuum.2015.05.012>.
30. Atta, A.A.; EL-Nahass, M.M.; Hassanian, A.M.; Elsabay, K.M.; EL-Raheem, M.M.A.; Alhuthali, A.; S.E.; Algamdi, M.S. Effect of thermal annealing on structural, optical and electrical properties of transparent Nb₂O₅ thin films. *Mater. Today Commun.* **2017**, *13*, 112-118, <https://doi.org/10.1016/j.mtcomm.2017.09.004>.
31. Korkmaz, S.; Pat, S.; Ekem, N.; Balbag, M.Z.; Temel, S. Thermal treatment effect on the optical properties of ZrO₂ thin films deposited by thermionic vacuum arc. *Vacuum* **2012**, *86*, 1930-1933, <https://doi.org/10.1016/j.vacuum.2012.05.002>.
32. Chandra Sekhar, M.; Kondaiah, P.; Mohan Rao, G.; Jagadeesh Chandra, S.V.; Uthanna, S. Post-deposition annealing influenced structural and electrical properties of Al/TiO₂/Si gate capacitors. *Superlattices and Microstructures* **2013**, *62*, 68-80, <http://dx.doi.org/10.1016/j.spmi.2013.07.001>.
33. Kim, J.; Haga, K.; Tokumitsu, E. Investigation of Nb-Zr-O Thin Film using Sol-gel Coating. *J. Semiconduct. Technol. Sci.* **2017**, *17*, 245-251, <https://doi.org/10.5573/JSTS.2017.17.2.245>.
34. Jagadeesh Chandra, S.V.; Mi-Ra, J.; Shim, K.H.; Hong, H.B.; Lee, S.H.; Ahn, K.S.; Choi, C.J. Effective Metal Work Function of Pt Gate Electrode in Ge Metal Oxide Semiconductor Device. *J Electrochem. Soc.* **2010**, *157*, H546-H550, <https://doi.org/10.1149/1.3332849>.
35. Jagadeesh Chandra, S.V.; Fortunato, E.; Martins, R.; Choi, C.J. Modulations in effective work function of platinum gate electrode in metal-oxide-semiconductor devices. *Thin Solid Films* **2012**, *520*, 4556-4558, <https://doi.org/10.1016/j.tsf.2011.10.137>.
36. Hayath Rajvee, Md.; Jagadeesh Chandra, S.V.; Rajesh Kumar, P.; Ramana, CH.V.V.; Neelama, K.; Dubey, R. S. Synthesis and Analysis of Zirconium Titanate Thin Films by using Sol-Gel Method. *Biointer. Res. Appl. Chem.* **2021**, *11*, 12761, <https://doi.org/10.33263/BRIAC115.1276112768>.